

Electronic Supplementary Information

Structural Basis of Single Molecular Heparin-FX06 Interaction Revealed by SPM Measurements and Molecular Simulations

Cunlan Guo,¹ Bin Wang,¹ Lianchun Wang,² Bingqian Xu^{1*}

¹Single Molecule Study Laboratory, Faculty of Engineering and Nanoscale Science and Engineering Center, ²Complex Carbohydrate Research Center and Department of Biochemistry and Molecular Biology, University of Georgia, Athens, GA 30602, USA.

*To whom correspondence should be addressed. E-mail: bxu@engr.uga.edu;

Table of Contents:

| | |
|---|----|
| SI-1. Significance of the Current Study..... | 3 |
| SI-2. Chemicals and Materials..... | 6 |
| SI-3. Immobilization of Heparin on Gold Substrate..... | 6 |
| SI-4. Functionalization of AFM Tip with PEG Linker and FX06..... | 7 |
| SI-5. AFM Imaging and Force-Distance Curve Measurement..... | 7 |
| SI-6. STM Imaging..... | 7 |
| SI-7. Comparison of STM Images and Simulated Heparin Structure..... | 8 |
| SI-8. Molecular Docking Using AutoDock Vina..... | 8 |
| SI-9. Calculation of Atomic Charge Distribution on HEP..... | 9 |
| SI-10. Simulation of Gibbs Free Energy Change (ΔG)..... | 9 |
| SI-11. Decomposing the Free Energy Contributions of FX06 Residues..... | 10 |
| SI-12. Comparison of Stretch Distance with Heparin Binding Mode on MUO Modified Gold Surface..... | 11 |
| Figure S1 to S8..... | 13 |
| Table S1 to S5..... | 21 |
| References and Notes..... | 26 |

SI-1. Significance of the Current Study.

Glycosaminoglycan heparan sulfate (HS) plays critical roles in many physiological and pathological processes ranging from embryonic development, angiogenesis, and blood coagulation to viral infection, inflammation and tumorigenesis¹. Heparin, the highly sulfated form of HS, is a commonly used anticoagulant in patients and has shown to also have non-anticoagulant functions, such as inhibition of tumor metastasis and inflammation²⁻⁵. The diverse biological activities of HS/heparin are rooted in their very heterogeneous structures^{1, 6, 7}. HS biosynthesis is a non-template-driven process in Golgi apparatus and initiated by polymerization of alternating hexuronic acid and D-glucosamine residues up to 200 disaccharides in length^{1, 6}. Following, the chains undergo a serial, step-wise modification reaction, including epimerization of a portion of the glucuronic acid residues to iduronic acid and addition of sulfate to some of the 2-*O*-positions of the hexuronic acid and *N*- and 6-*O*-positions of N-acetylglucosamine residues. Importantly, the accumulative action of the modifications is incomplete and occurs in cluster in N-sulfated regions, generating heterogeneous sulfate pattern and a defined HS domain structure composed of highly (S-domains), partially (transition zones), and nonsulfated regions. The heterogeneous sulfation pattern in combination with the domain structure forms numerous docking sites, enabling HS/heparin to interact and modulate a remarkable number of biologically important proteins, including proteinases, proteinase inhibitors, growth factors, morphogen, chemokines, adhesion molecules, etc^{6, 7}.

Understanding the interaction of HS/heparin with the biologically important proteins has been the key to elucidate their diverse biological functions⁶⁻⁹. Several methods have been developed to study HS/heparin-protein interactions, including affinity chromatography, analytical ultracentrifugation, electrophoretic mobility shift assay, competition experiments, mass spectrometry-based approaches, isothermal titration calorimetry and surface plasmon resonance⁹⁻¹⁵. Although powerful, these approaches are often low throughout, labor intensive and require significant quantities of HS and heparin/or protein. To elucidate the HS/heparin structure required for interaction with proteins, these existing methods often require oligosaccharides or polysaccharides that are relatively homogenous in chain length and charge density, as fractionated heparin or chemically modified HS. However,

these well-prepared oligosaccharides are still structurally heterogeneous and in general are unable to provide precise structure information of HS/heparin for the interaction. Recently, a microarray assay was developed using synthesized tetrasaccharide with defined sulfation sequence to examine HS-protein interaction and has provided a general, facile mean to indentify new HS-protein interaction and to determine HS structure interacting with protein¹⁶. However, many HS/heparin-interacting proteins require a size of HS/heparin larger than tetrasaccharide to interact with, for example, the well-studied heparin-binding protein antithrombin⁶⁻⁸. Meanwhile, the available structures of synthesized tetrasaccharides are very limited^{2, 5, 17-19}. Therefore, the structural studies of HS/heparin-protein interactions have been still difficult, limited by the complexity and heterogeneity of naturally occurring HS/heparin. A method to examine the HS/heparin-protein interaction at single molecular level in combination with computational modeling may overcome these limitations to unbiasly determine the interaction and the HS/heparin structure required for the interaction.

Single molecule interactions have been measured by using very sensitive force probes including the optical trap force probe (OTFP)²⁰⁻²³ and the biomembrane force probe (BFP)²⁴⁻²⁶. Controlled by laser power and pipette suction pressure, the spring constants of OTFP and BFP can be tuned in a range of 10^{-3} - 10^{-1} pN/nm and 0.1-1pN/nm, respectively, making these methods especially well-suited for probing relatively small interactions between biomolecules. However, neither OTFP nor BFP offer high resolution imaging. With its ability to observe, manipulate and explore the functional components of the biological molecules at subnanometer resolution, scanning probe microscopy (SPM) has been developed to a multifunctional 'lab-on-a-tip' technology²⁷. In addition to high resolution imaging of proteins, nucleotides, membranes, and living cells²⁸, the measurement of mechanical forces at the molecular level provides detailed insights into the function and structure of biomolecular systems²⁹. Inter- and intramolecular interactions can be studied directly at the molecular level, as exemplified by the analysis of polysaccharide elasticity³⁰, DNA mechanics^{23, 31}, the function of molecular motors³², and the binding potentials of receptor–ligand pairs involved in cell adhesion³³. To establish the molecular bases of the single molecular interactions to interpret the experimentally measured data, computer simulations are well-suited to address these issues^{34, 35}.

Therefore, a combination of experimental efforts with computer simulations will offer a full mechanistic understanding that includes key structural and dynamic features.

Ischemia/reperfusion-elicited tissue injury contributes to morbidity and mortality in a wide range of pathologies, including myocardial infarction, ischemic stroke, acute kidney injury, trauma, circulatory arrest, sickle cell disease and sleep apnea³⁶. Ischemia/reperfusion injury is also a major challenge during organ transplantation and cardiothoracic, vascular and general surgery³⁶. Inflammation and the inflammation-triggered subsequent coagulation play central roles in the reperfusion injury^{36, 37}. Targeting both inflammation and coagulation, the dual function model, represents a new direction to develop effective treatment of ischemia/reperfusion-elicited tissue injury³⁷. The fibrin-derived peptide B β 15-42 (FX06), a naturally occurring, 28-amino acid product cleaved from fibrin fragments³⁸, has shown to protect from myocardial infarction and acute injuries of lung and kidney in animal models³⁹⁻⁴¹. Very recently, a multi-centered phase II clinical trial study concluded that FX06 effectively protects patients with acute myocardial infarction⁴², exhibiting a promising potential to develop FX06 as a novel drug for treatment of ischemic/reperfusion-related human diseases. Parts of this beneficial effect may be explained by attenuating inflammation and preserving vascular barrier functions during shock via interaction with VE-cadherin. Meanwhile, FX06 has been observed to bind heparin and fibrin essentially requires to expose the FX06 sequence to promote endothelial cell adhesion, spreading and proliferation⁴³⁻⁴⁹, suggesting that FX06 may interact with endothelial HS to promote the cell functions to attenuate vascular injury and to enhance vascular repair, representing another mechanism underlying the protective effect in ischemic-reperfusion injury. Furthermore, heparin is commonly administered to prevent or treat thrombosis^{2, 5}, a pathological condition with elevated levels of FX06 in patients⁴⁵, at this clinical situation the interaction with FX06 may enhance the anticoagulant and anti-inflammatory effect of heparin, contributing its protective effect on reperfusion injury. In depth understanding the interaction between heparin/HS and FX06 will have significant impact on our interpretation of the roles of FX06 in tissue repair, heparin-modulated coagulation and anti-inflammation as well as in its general protective effect in ischemic-reperfusion injury.

In this study, we applied SPM-based technology in combination with computational modeling to unambiguously reveal the molecular bases of heparin-FX06 single molecule interactions, which offered a full mechanistic understanding that includes key structural and dynamic features.

SI-2. Chemicals and Materials.

Heparin (Mw range 12000-14000, average molecular weight 13500) was purchased from Scientific Protein Laboratories. FX06 with the sequence of GHRPLDKKREEAPSLRPAPPPISGGGYR was synthesized and purified by GenScript. PEG linker ((thiol-(polyethylene glycol)-acid, HS-PEG-COOH, Mw 2000) was purchased from Creative PEGWorks. The other chemicals, N-hydroxysuccinimide (NHS), 1-(3-dimethyl aminopropyl)-3-ethylcarbodiimide hydrochloride (EDC), 11-mercapto-1-undecanol (MUO), 1-dodecanethiol, and diglyme, were purchased from Sigma-Aldrich, while epichlorohydrin was from TCI America. All chemicals were directly used without further purification.

SI-3. Immobilization of Heparin on Gold Substrate.

The gold substrate was prepared by thermally evaporating gold layer on freshly cleaved mica surface. Before the experiment, the substrate was annealed with hydrogen flame to form Au(111) flat surface and used immediately. Heparin was immobilized on gold substrate according to a reported method with some modifications (Fig. S1)⁵⁰. MUO solution (5 mM in DMSO) was first used to treat gold substrate for 5 hours at room temperature to form a monolayer with hydroxyl groups on gold surface. After thoroughly washing with ethanol and water, the resulted hydrophilic surface reacted with epichlorohydrin (0.6 M) in a mixture solution (1:1 (v:v) of diglyme and 0.4 M NaOH) for 4 hours at room temperature, which introduced active epoxy groups as electrophilic coupling sites at the terminal hydroxyl group of MUO on gold surface. Followed by washing with water, ethanol and water, the substrate was treated with heparin solution (0.2 mM heparin in 0.1 M NaOH) overnight at room temperature. Under alkaline condition, heparin was covalently connected to the epoxy groups at the MUO terminal by the hydroxyl groups of heparin sugar rings. Finally, the sample surface was rinsed with water, and stored in PBS for further measurement.

SI-4. Functionalization of AFM Tip with PEG Linker and FX06.

Bare silicon (Si) AFM tips (Nanoscience Instruments) were first cleaned under UV/ozone for 15 min at both sides, respectively. And then, the cleaned tips were coated with the magnetic material and gold by using an E-beam evaporator. These coated tips were further functionalized by using the protocol previously established in our group⁵¹ but with some modification. Briefly, the tips were immersed in a DMSO solution containing 0.5 mM PEG linker and 0.2 mM 1-dodecanethiol for 6 hours. Mixed monolayer then formed on the tip surface through the mercapto-Au reaction, which had a low density PEG linker with exposed carboxyl group. After rinsing with DMSO and water, the carboxyl groups were activated to form N-hydroxysuccinimidyl ester by reacting with 10 mM fresh EDC/NHS mixture solution for 30 min. Then the tips were further thoroughly washed with phosphate buffered saline (PBS, pH 7.4) and dipped into FX06 solution (20 μ M, in PBS) overnight. FX06 was linked on AFM tip by the reaction between its amino group and N-hydroxysuccinimidyl ester. Functionalized tips were stored in PBS before use.

SI-5. AFM Imaging and Force-Distance Curve Measurement.

All AFM experiments including imaging, molecular recognition, and force-distance curve measurement were carried out with an Agilent 5500 AFM system (Agilent, Chandler, AZ). Silicon cantilevers tips with spring constant of around 0.1 N/m were used for experiments. All the images were obtained in PBS buffer and recognition images were acquired by using Agilent magnetic AC (MAC) mode AFM with a magnetically coated cantilever. After imaging, the force-distance curves of FX06 and heparin were measured at eight loading rates. For each loading rate, more than 300 curves were collected to analyze the force distribution, the most probable rupture force as well as the variation of stretch distance. The data analysis was achieved by a homemade LabView computer program.

SI-6. STM Imaging.

A PicoPlus SPM system (Molecular Imaging) with a PicoScan 3000 Controller (Molecular Imaging) was used for STM imaging. Sheared gold wire with diameter of 0.25 mm (99.999%, Alfa Aesca) was coated with wax as a STM tip. The STM images were obtained in PBS buffer under relatively

high voltage and low current to minimize potential sample damage. The obtained AFM and STM images were processed by WSxM software⁵².

SI-7. Comparison of STM Images and Simulated Heparin Structure.

The STM topography image of heparin was enlarged to show detailed features of heparin chain structure in Fig. S4. The simulated heparin structure was the fragment randomly picked, including residue 5, 6, 7, 8, 9, 10, and 11 in the model 1 of PDB entry 3IRJ⁵³. Four oxygen-oxygen distances were measured in the simulated structures in Fig. S4a and the values were labeled. The corresponding cross-section profiles were measured in STM image and listed through x1 to x4. In PDB entry 3IRJ model 1, the repeating unit N,O6-disulfo-glucosamine was named SGN, and the O2-sulfo-glucuronic acid was named IDS. The four distances measured in the model were O5S(SGN5)-O3S(SGN7) (x1), O5S(SGN7)-O2S(SGN9) (x2), O61(IDS8)-O1S(IDS10) (x3), and O62(IDS10)-O6S(SGN11) (x4). The values of these distances obtained from simulation were x1=6.83 Å, x2=5.73 Å, x3=7.65 Å, x4=7.82 Å (Fig. S4a) and the distance measured from the cross-section profiles were x1=6.8 Å, x2=5.7 Å, x3=7.6 Å, x4=7.6 Å (Fig. S4c). These corresponding values from simulation and cross-section profile were very close to each other, which proved that the topography image observed in STM was part of the heparin filament structure.

SI-8. Molecular Docking Using AutoDock Vina.

The program AutoDock vina was used to predict the docking conformation from the FX06 folded structure (FX06) and the heparin five consecutive sugar units structure (HEP)⁵⁴. The interaction between FX06 and heparin is among the most interesting protein-carbohydrate interactions that has drawn increasing attentions in both experimental and simulation researches. AutoDock vina is a new docking program similar to AutoDock but has higher performance and is easier to use. It is good at docking of biomolecules, such as proteins, nucleic acids, and carbohydrates. Therefore, we used this program to predict the complex structure (COM). HEP (Fig. S2a, highlighted in stick representation) was used as the ligand, which was treated to allow some groups moving flexibly during the docking. The simulated FX06 (Fig. S2b) was used as the receptor. In AutoDock vina, the grid box was set to cover entire FX06 surface. The final COM structure was the most stable conformation (Fig. S2c)

picked from the series of predicted conformations.

To complement the experimental data and get better understanding of their interactions, we analyzed the possible interactions between FX06 and HEP at their interface. The hydrogen bonds and electrostatic interactions are usually the major contributions in biomolecular interactions. The electrostatic interactions have both long-range and short-rang effects but hydrogen bonds have more distinguishable bond form in local region. In VMD visualization software, the default setting for the hydrogen bonds are: distance cutoff 3.0 Å, angle cutoff 20°⁵⁵. Based on these criteria, six hydrogen bonds were found, including H(HIE2):O(NHSO3-), O(HIE2):H(-OH), H(LYS7):O(-CH2OSO3-), H(ARG9):O(-CO2-), H(ARG9):O(-CO2-), and H(ARG28):O(α -glycosidic-O-). Their bond lengths and bond angles were 1.89 Å and 168.32°, 1.85 Å and 170.85°, 1.90 Å and 165.91°, 1.64 Å and 172.86°, 1.71 Å and 172.50°, 1.75Å and 166.81°, respectively. These parameters indicated that the six hydrogen bonds were very stable and played important roles in the binding/unbinding.

SI-9. Calculation of Atomic Charge Distribution on HEP.

The R.E.D. Server provides the quantum mechanics software and protocols to calculate restrained electrostatic potential (RESP) or electrostatic potential (ESP) derived atomic charge and to build force field library, which are especially useful for the simulation of non-standard molecular fragment(s)^{56, 57}. The heparin fragments #1 - #5 (Fig. S8) were cut from the HEP structure, and special neutral groups were added to each fragment as restraints to form five complete molecules. On the R.E.D. server, the R.E.D. IV Mode 1, RESP-C2 charge model, and Gaussian 2009 A.02 were chosen to calculate the charge distribution on each molecule⁵⁸. Consequently, the neutral groups were removed and the charges distributions for these five fragments were obtained. The HEP structure was rebuilt from the five fragments and the partial charge values of all atoms were input into AMBER to do further simulation⁵⁹. The calculated charge value of each atom on HEP structure was shown in Table S2. These charge values were used for docking and binding energy simulation.

SI-10. Simulation of Gibbs Free Energy Change (ΔG).

In AMBER XLEaP, the COM structure was neutralized with Na⁺ ions and put into a water solvate box TIP3PBOX (12.0 Å long range cutoff). This solvated COM was minimized, heated to 300 K in

constant volume, and equilibrated at 300 K in constant pressure. The equilibration phase for 0.5 ns was simulated. The next step was the production phase simulation, which took 13 ns. We checked the RMSD of the production phase trajectories during every 1 or 2 ns and found that the RMSD values showed some stable plateaus during certain period of time but fluctuations during other time periods. We used MMPBSA.py (molecular mechanic/Poisson-Boltzmann surface area) to calculate Gibbs free energy change based on several simulation time of production phase⁵⁹. The 300 snapshots from the trajectories during 12.1 and 12.4 ns (simulated time period) generated the ΔG value of -14.3721 ± 29.637 kcal/mole, which was very close to the experimental result. The ionic strength used in the calculation was estimated as 0.15 M since the buffer used for force spectroscopy was 0.1 M NaCl and 0.01 M PBS. The output file of the MMPBSA.py is shown in Table S3. In gas phase, the electrostatic contribution (EEL, -1333 kcal/mol) is very large compared to van der Waals contribution (VDWAALS, -1.36 kcal/mol); and in solvated phase, the electrostatic contribution (EPB, 1323 kcal/mol) is also large compared to nonpolar contribution (ECAVITY, -3.26 kcal/mol). Therefore, electrostatic interaction plays important roles in the binding/unbinding process because it has both long-range and short-range effects.

SI-11. Decomposing the Free Energy Contributions of FX06 Residues.

The MMPBSA pre-residue energy decomposition calculated the energy contributions from HEP (used as one residue) and each amino acid residue in FX06 to the entire binding energy of COM. The results of pre-residue decomposition based on Poisson Boltzmann solvent model are shown in Table S4. The ligand UNK1 represents the HEP structure. Its five consecutive sugar residues are highly negatively charged, so UNK1 shows the biggest value on the electrostatics term. FX06 residues GLY1, ARG3, LYS7, LYS8, ARG9, ARG16, and ARG28 contributed relatively large negative values on electrostatics term. All these residues carried positive charges (GLY1 was the N-terminal), so they reduced the free energy when they interacted with highly negatively charged HEP (residue UNK1 in Table S4). On the contrary, FX06 residues ASP6, GLU10, and GLU11 showed relatively large positive values on electrostatics terms, which indicated that these residues increased the free energy after binding to HEP. This energy increase was due to the repulsion of negative

charges. For the per-residue total energy change, FX06 residues ARG3, PRO4, LYS7, LYS8, ARG9, and ARG16 contributed the most, which meant that these residues played key roles in the FX06-HEP interactions. The major contribution of PRO4 was from the van der Waals term, while the contributions of other residues were mostly from the electrostatics term. The pairwise decomposition was also conducted using MMPBSA.py script. As shown in Table S5, the negative binding energies were mainly contributed from residue pairs of HEP-GLY1, HEP-HIE2, HEP-ARG3, HEP-PRO4, HEP-LYS7, HEP-LYS8, HEP-ARG9, HEP-ARG16, and HEP-ARG28. Overall, these energy decomposition results agree with the force analysis in the discussion section.

SI-12. Comparison of Stretch Distance with Heparin Binding Mode on MUO Modified Gold Surface.

In the force spectroscopy measurements, the PEG linker used for connecting FX06 with the AFM tip was around 15 nm in length (estimated from the simulated PEG linker molecular structure, PDB entry 15P). It was close to the short stretch distance (15 ± 1.9 nm) obtained from the contour map. On the other hand, the STM measured length of heparin molecule was 16.50 ± 1.80 nm. The total length of PEG linker and heparin molecule approximately equaled to 31 nm, which was close to the long stretch distance (29 ± 1.9 nm) on the contour map. The different stretch distances may be caused by the varying degrees of heparin immobilization on MUO modified gold surface. The heparin sugar unit contains hydroxyl groups that can react with epoxy-alkanethiols on MUO monolayer for immobilization⁵⁰. Under our experimental conditions, the heparin molecules could react with MUO monolayer through different number of hydroxyl groups (inset in Fig. 4a). For some heparin molecules, the filament might link with MUO monolayer only by one hydroxyl group at one end of heparin sugar units, which would give the longest stretch distance in force-distance curve. Some heparin filaments might be completely fixed on MUO monolayer or immobilized on MUO monolayer through both sides of the filaments, so the stretch distance would only reflect the length of PEG linker. For some heparin molecules, the filaments might connect with MUO molecules through parts of hydroxyl groups, which would result in diverse stretch distances ranging between the longest and shortest values. On the other hand, one FX06 molecule could bind to one of

any five consecutive sugar units on one heparin filament, which would also generate various stretch distances. Furthermore, due to different degrees of heparin immobilization on MUO monolayer as well as the multiple binding sites on heparin filament for FX06, short stretch distances showed greater proportion in the total measured stretch distance.

Moreover, the event distribution of both rupture force and stretch distance showed intriguing phenomena with the increase of loading rates (Fig. S7). With the loading rate increasing from 10 nN/s to 403 nN/s, the stretch distance distribution shifted from the region of 15 ± 1.9 nm - 29 ± 1.9 nm to the region of 9 ± 1.0 nm - 19 ± 1.0 nm, associated with the force increasing from 11.77 pN to 57.16 pN (Table S1). Meanwhile, the event distribution became broadening concomitant with the increasing loading rate. For this AFM assisted heparin-FX06 reaction, the force spectroscopy at a certain loading rate displayed the rupture force and stretch distance at their non-equilibrium state. With the loading rate increased, the force-distance curves related binding/unbinding processes were driven far away from the equilibrium state. These non-equilibrium processes could result in broader distribution of both rupture forces and stretch distances. Meanwhile, high loading rates brought more extra energies to the heparin-FX06 complex during the binding/unbinding processes, which made the complex less stable to dissociate easily at a shorter stretch distance.

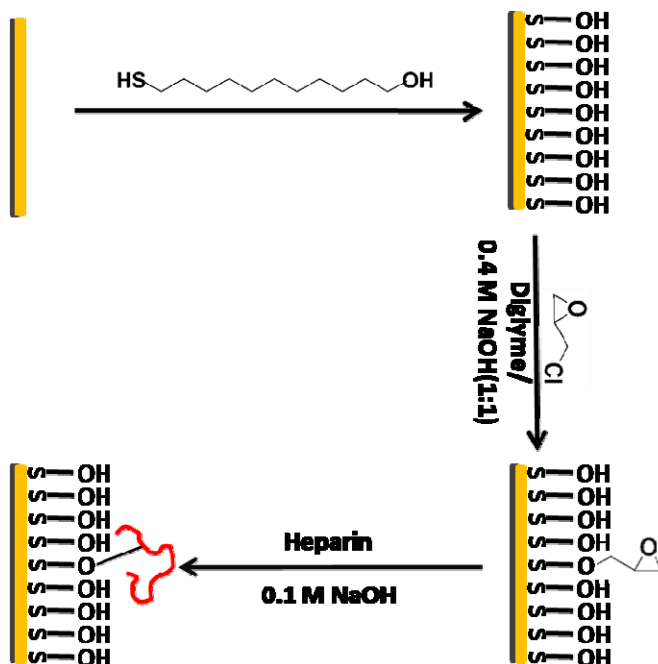


Figure S1. Schematic of the procedure for covalently immobilizing heparin on a MUO monolayer modified gold surface.

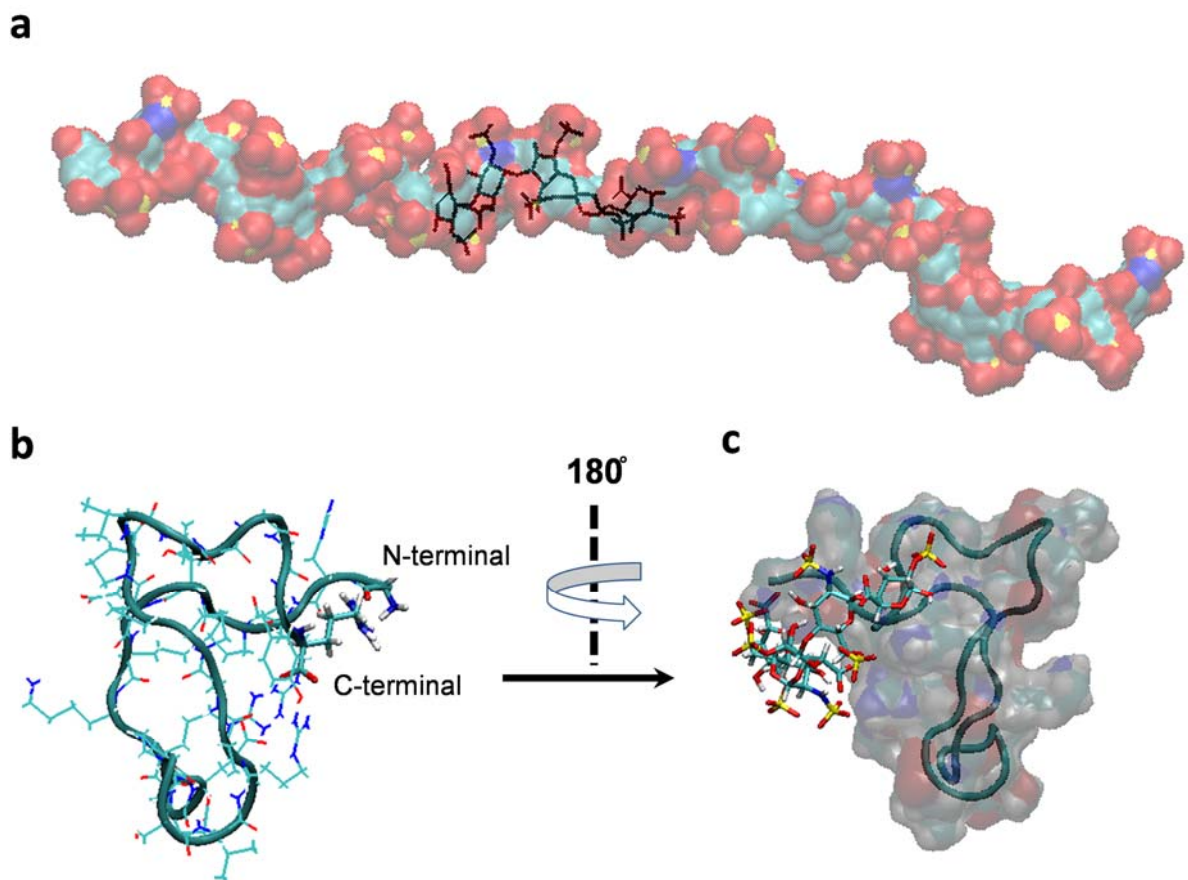


Figure S2. The simulated structures of heparin, FX06, and their binding complex. **a**, A representative heparin structure (24 sugar units) obtained from literature (PDB entry 3IRJ, model 1). The heparin used in experiments is longer (with around 46 sugar units) but still remains linear as proved in Fig. 1c, so it has opening sites for FX06 binding. The stick representation highlights the five consecutive sugar units used for docking simulation. **b**, Folded tertiary structure of FX06 generated by AMBER molecular dynamics, both backbone and side chains are shown. **c**, The most stable binding complex predicted by AutoDock vina. The five consecutive sugar units (shown in stick representation) are embedded into a shallow groove of FX06 (shown in backbone and surface representation). **b** and **c** are shown in the same scale, but different from **a**.

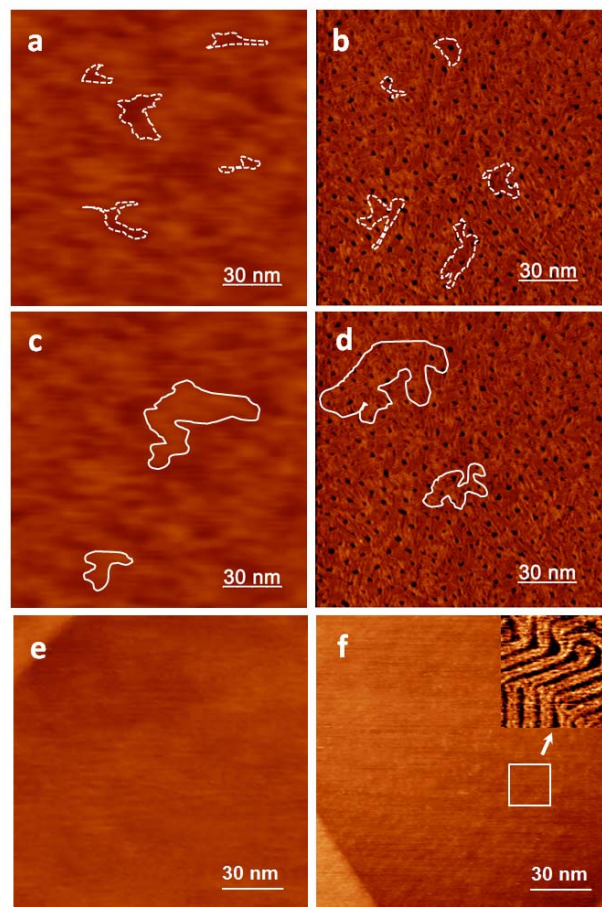


Figure S3. Comparison of topographic images obtained from AFM and STM. Images on the left (**a** and **c**) are the same AFM topographic images measured by FX06 modified AFM tip. Images on the right (**b** and **d**) are the same STM topographic images. Dashed white lines indicate the area of MUO monolayer without being covered by heparin. Solid lines show the area covered by heparin filaments. **e** shows the AFM image of bare Au(111) surface in PBS buffer, without any molecule modification. **f** is the STM image of bare Au(111) surface without any molecule modification. The insert STM image in **f** was enlarged from a small area of 20 nm by 20 nm (white frame), with z range of 0.3 nm, and shows the reconstructed Au atomic layers. The z range for AFM topographic image is 1.56 nm, and the z range for STM topographic image is 1.52 nm.

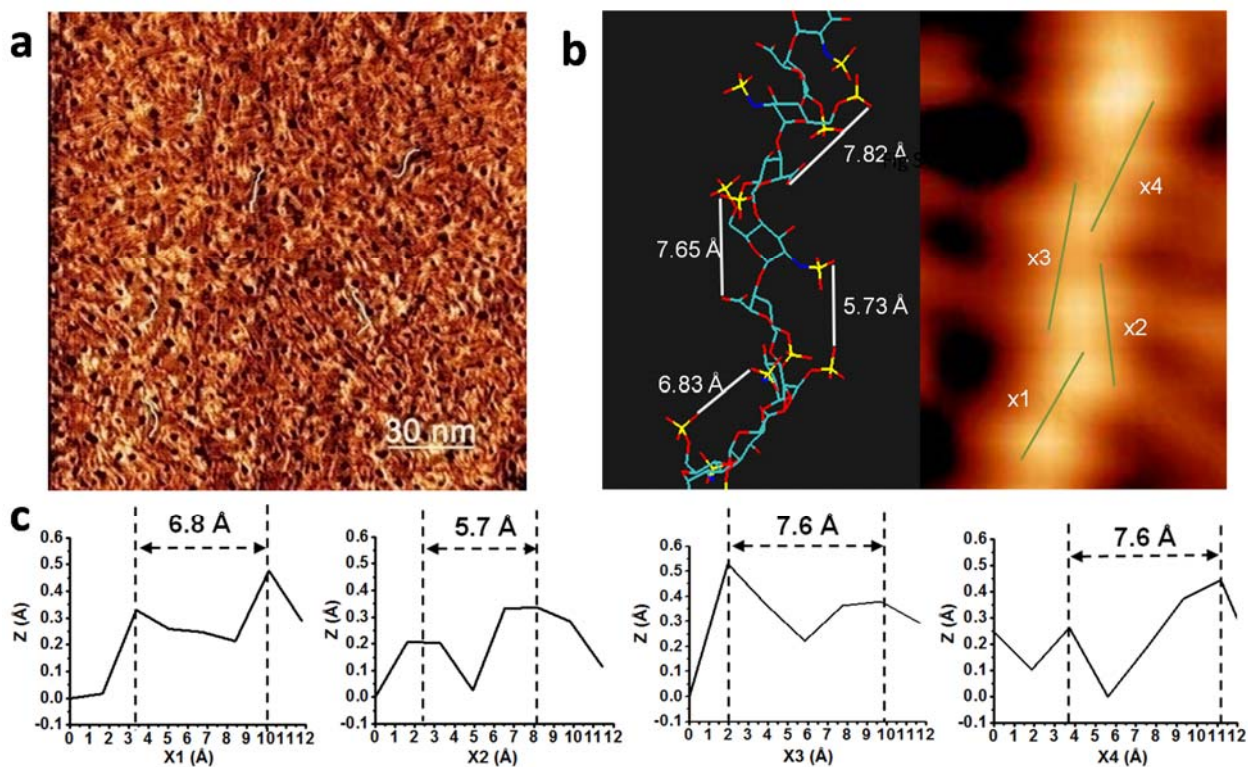


Figure S4. Comparison of high resolution STM image and simulated structure of heparin on Au(111) surface. **a**, STM image of heparin molecules on MUO monolayer. The z range is 0.35 nm. **b**, Left is the heparin structure from an entire heparin molecule (PDB entry 3IRJ model 1). Labels show the distances between two oxygen atoms on the sugar units. Right is an enlarged area of the middle part of a heparin molecule from STM topography image. The four green lines mark the places where cross-section profiles were measured. **c**, The cross-section profiles of four measurements x1, x2, x3, and x4, which are corresponding to the green marked places in **b**.

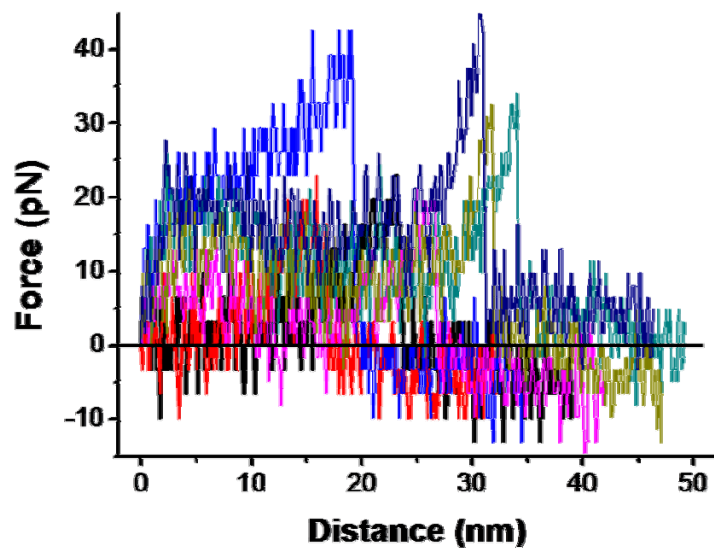


Figure S5. Seven typical force-distance curves selected from the 20 curves used for the calculation of Gibbs free energy change at the equilibrium state. For each curve, (0, 0) was set in the retracting process where the tip just fully recovered from upward bending.

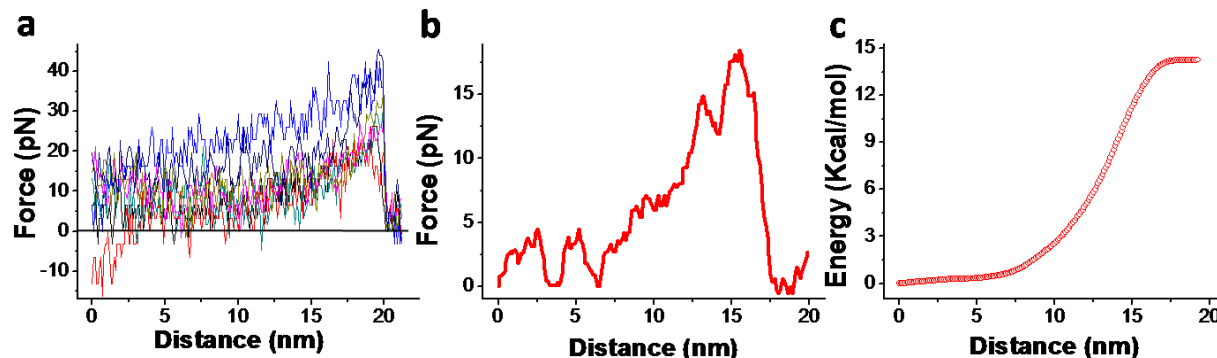


Figure S6. Calculation of Gibbs free energy change at equilibrium state. **a**, Seven typical force-distance curves selected from the 20 curves used for the calculation of Gibbs free energy change at equilibrium state. For each curve, the distance part without obvious force signal come from the pulling of PEG linker or part of unfixed heparin filament. This part of stretch distance may not relate to the complex breakage and was removed. **b**, Corresponding mean force-distance curve obtained by averaging 20 curves using weighted work integral averaging. **c**, Corresponding reconstructed Gibbs free energy for heparin-FX06 interaction. The value of Gibbs free energy change was calculated to be 14.24 Kcal/mol.

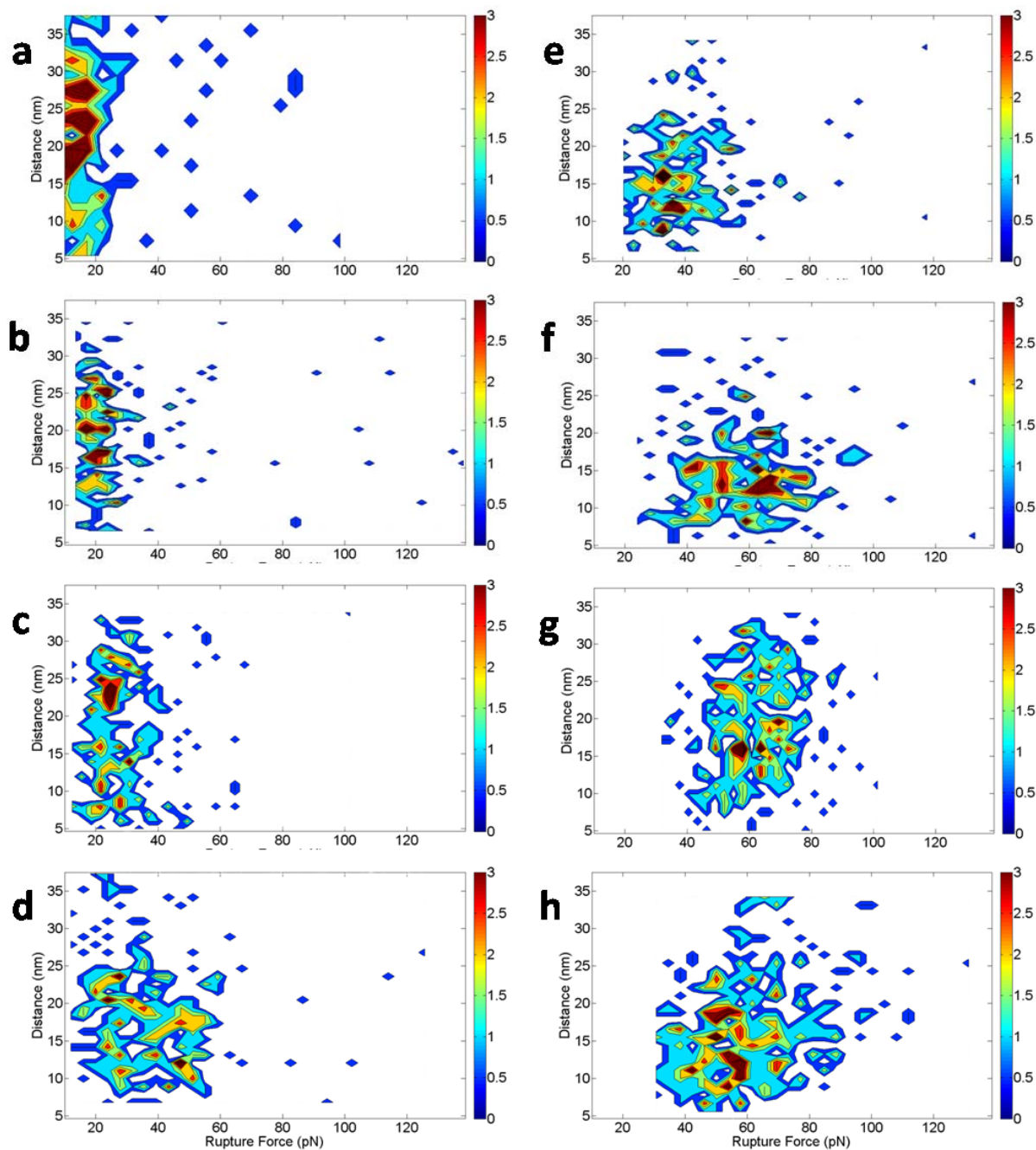


Figure S7. 2D event distribution plots associated with both rupture force and stretch distance at different loading rates: **a**, 10 nN/s; **b**, 15 nN/s; **c**, 24 nN/s; **d**, 40n N/s; **e**, 80 nN/s; **f**, 160 nN/s; **g**, 245 nN/s; **h**, 403 nN/s. Different colors indicate the proportions of rupture force obtained with certain stretch distance.

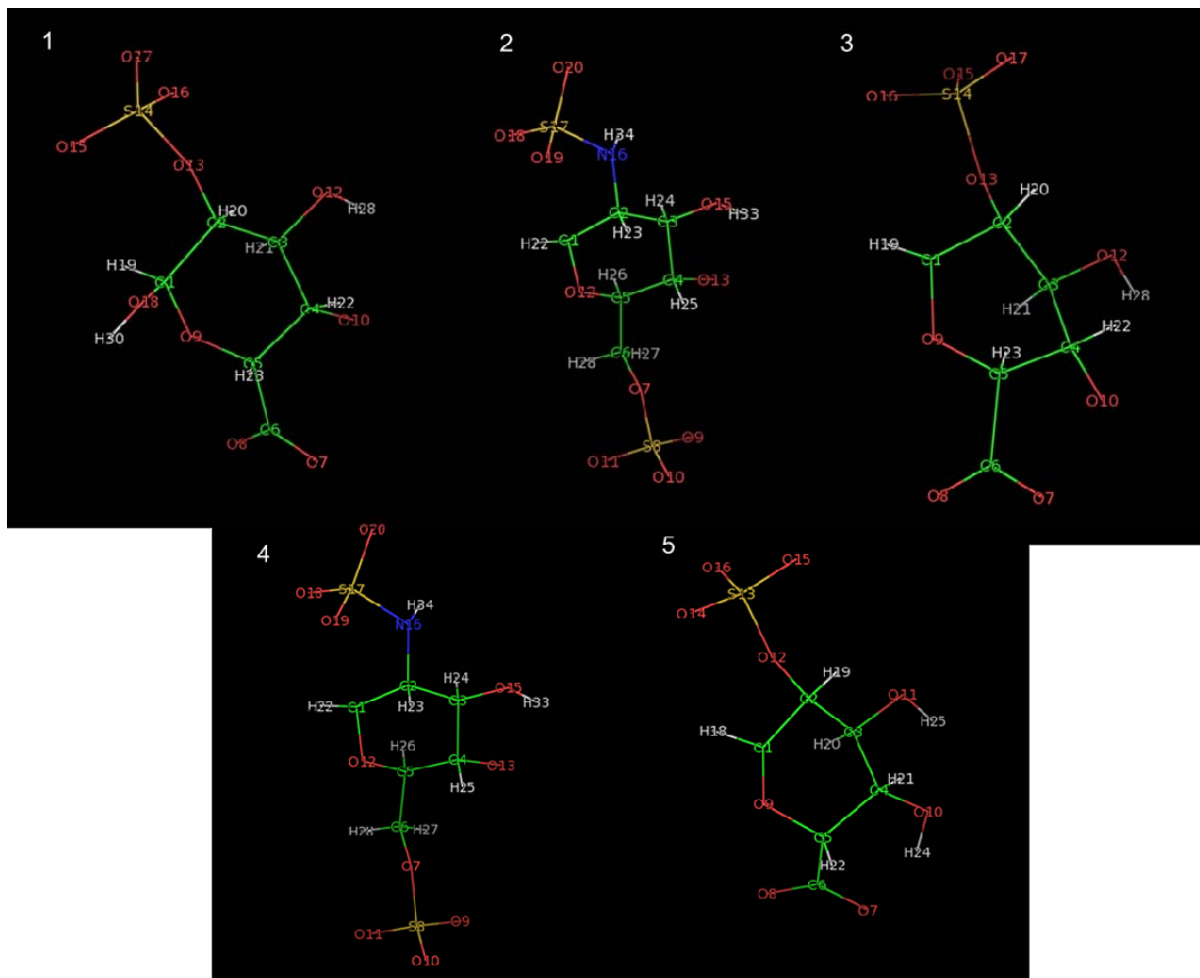


Figure S8. The fragments of HEP used for the simulation of RESP charges. Units 1 to 5 were derived from the entire HEP structure and uploaded to R.E.D. server to calculate the atom charges. The labels show the atom names on each unit when RESP charges were calculated.

Table S1. The most probable rupture forces under different force loading rates.

| <i>r</i> (nN/s) | 10 | 15 | 24 | 40 | 80 | 160 | 245 | 403 |
|--------------------|--------|--------|--------|---------|---------|---------|---------|---------|
| F* | 11.77 | 19.79 | 24.7 | 34.57 | 35.95 | 55.53 | 59.79 | 57.16 |
| (pN) | ± 6.72 | ± 4.83 | ± 8.22 | ± 16.90 | ± 12.29 | ± 18.98 | ± 13.39 | ± 18.17 |

Table S2. Partial charge values for each atoms in HEP structure.

| Unit number | 1 | 2 | 3 | 4 | 5 |
|-------------|--------------|---------------|--------------|---------------|--------------|
| Atom name | C1: 0.3761 | C1: 0.0755 | C1: 0.2173 | C1: 0.0785 | C1: 0.1035 |
| and charge | C2: 0.4106 | C2: 0.0771 | C2: 0.4891 | C2: 0.0785 | C2: 0.3998 |
| value | C3: 0.1230 | C3: 0.1725 | C3: 0.1223 | C3: 0.1703 | C3: 0.2228 |
| | C4: 0.1764 | C4: 0.0806 | C4: 0.1894 | C4: 0.0799 | C4: 0.1614 |
| | C5: 0.3458 | C5: 0.2686 | C5: 0.3278 | C5: 0.2690 | C5: 0.2082 |
| | C6: 0.8123 | C6: 0.0106 | C6: 0.8185 | C6: 0.0108 | C6: 0.8508 |
| | O7: -0.8071 | O7: -0.4059 | O7: -0.8091 | O7: -0.4057 | O7: -0.8042 |
| | O8: 0.8071 | S8: 1.3090 | O8: -0.8091 | S8: 1.3087 | O8: -0.8042 |
| | O9: -0.5770 | O9: -0.6852 | O9: -0.5354 | O9: -0.6851 | O9: -0.4561 |
| | O10: -0.4534 | O10: -0.6852 | O10: -0.4586 | O10: -0.6851 | O10: -0.6909 |
| | O12: -0.6644 | O11: -0.6852 | O12: -0.6750 | O11: -0.6851 | O11: -0.7069 |
| | O13: -0.5114 | O12: -0.3856 | O13: -0.5216 | O12: -0.3867 | O12: -0.5051 |
| | S14: 1.3304 | O13: -0.5136 | S14: 1.3298 | O13: -0.5093 | S13: 1.3493 |
| | O15: -0.7009 | O15: -0.6622 | O15: -0.7008 | O15: -0.6618 | O14: -0.7061 |
| | O16: -0.7009 | N16: -0.6723* | O16: -0.7008 | N16: -0.6723* | O15: -0.7061 |
| | O17: -0.7009 | S17: 1.2929 | O17: -0.7008 | S17: 1.2927 | O16: -0.7061 |
| | O18: -0.7560 | O18: -0.6917 | H19: 0.0973 | O18: -0.6917 | H18: 0.1459 |
| | H19: 0.0565 | O19: -0.6917 | H20: 0.0501 | O19: -0.6917 | H19: 0.0759 |
| | H20: 0.0672 | O20: -0.6917 | H21: 0.0393 | O20: -0.6917 | H20: 0.0373 |
| | H21: 0.0408 | H22: 0.1591 | H22: -0.0185 | H22: 0.1582 | H21: 0.0224 |
| | H22: -0.0179 | H23: 0.1583 | H23: -0.0627 | H23: 0.1577 | H22: -0.0306 |
| | H23: -0.0655 | H24: 0.0736 | H28: 0.3909 | H24: 0.0735 | H24: 0.3727 |
| | H28: 0.3869 | H25: 0.0882 | | H25: 0.0888 | |
| | H30: 0.4617 | H26: 0.0248 | | H26: 0.0245 | |
| | | H27: 0.0802 | | H27: 0.0802 | |
| | | H28: 0.0802 | | H28: 0.0802 | |
| | | H33: 0.4041 | | H33: 0.4042 | |
| | | H34: 0.3346 | | H34: 0.3348 | |

*: The initial overall charge value of HEP is -9.9998. To make the charge value an integral for further simulation, the charge values of nitrogen atoms were changed from -0.6722 to -0.6723. Therefore, the overall charge value for HEP is -10.0000 in the later docking and binding energy simulations.

Table S3. The simulation results of Gibbs free energy change (ΔG binding) by using MMPBSA.py and Poisson Boltzmann model.

| POISSON BOLTZMANN: | | | |
|---|--------------|-----------|-------------------|
| Complex: | | | |
| Energy Component | Average | Std. Dev. | Std. Err. of Mean |
| VDWAALS | -85.0008 | 28.4236 | 1.6383 |
| EEL | -1778.9550 | 57.5159 | 3.3152 |
| EPB | -1595.3109 | 55.1679 | 3.1798 |
| ECAVITY | 17.8697 | 0.3819 | 0.0220 |
| G gas | -1863.9558 | 67.9364 | 3.9158 |
| G solv | -1577.4412 | 54.9149 | 3.1652 |
| TOTAL | -3441.3970 | 30.3393 | 1.7487 |
| Receptor: | | | |
| Energy Component | Average | Std. Dev. | Std. Err. of Mean |
| VDWAALS | -66.5212 | 5.1954 | 0.2995 |
| EEL | -1454.6307 | 27.6866 | 1.5958 |
| EPB | -707.1897 | 20.1287 | 1.1602 |
| ECAVITY | 15.0165 | 0.2314 | 0.0133 |
| G gas | -1521.1519 | 27.0528 | 1.5593 |
| G solv | -692.1732 | 20.1806 | 1.1632 |
| TOTAL | -2213.3251 | 13.2185 | 0.7619 |
| Ligand: | | | |
| Energy Component | Average | Std. Dev. | Std. Err. of Mean |
| VDWAALS | -17.1222 | 4.2395 | 0.2444 |
| EEL | 1008.7372 | 23.0273 | 1.3273 |
| EPB | -2211.4285 | 18.4854 | 1.0655 |
| ECAVITY | 6.1138 | 0.1097 | 0.0063 |
| G gas | 991.6149 | 24.4217 | 1.4076 |
| G solv | -2205.3147 | 18.5631 | 1.0700 |
| TOTAL | -1213.6998 | 9.9888 | 0.5757 |
| Differences (Complex - Receptor - Ligand): | | | |
| Energy Component | Average | Std. Dev. | Std. Err. of Mean |
| VDWAALS | -1.3573 | 28.3471 | 1.6339 |
| EEL | -1333.0615 | 79.4930 | 4.5819 |
| EPB | 1323.3073 | 76.2979 | 4.3977 |
| ECAVITY | -3.2606 | 0.2454 | 0.0141 |
| DELTA G gas | -1334.4189 | 91.1805 | 5.2556 |
| DELTA G solv | 1320.0467 | 76.1253 | 4.3878 |
| DELTA G binding = | -14.3721 +/- | 29.6377 | 1.7083 |

Table S4. The pre-residue decomposition of binding energy.

| | Residue | Internal (kcal/mol) | van der Waals (kcal/mol) | Electrostatics (kcal/mol) | Polar Solvation (kcal/mol) | Non-polar Solvation (kcal/mol) | Total (kcal/mol) |
|-----------------|---------|------------------------|-----------------------------|------------------------------|----------------------------------|--------------------------------------|---------------------|
| Ligand | UNK1 | 0.000±15.182 | -0.679±14.791 | -666.531 ±41.228 | 666.696±37.569 | 0.000±0.000 | -0.514±59.670 |
| Receptor | GLY1 | 0.000±2.904 | 1.762±5.696 | -199.613 ±9.291 | 198.967 ±8.867 | 0.000±0.000 | 1.116±14.347 |
| | HIE2 | 0.000±4.093 | -1.500±1.953 | 6.783±4.066 | -5.791±2.163 | 0.000±0.000 | -0.507±6.464 |
| | ARG3 | 0.000±5.905 | -2.146±1.968 | -200.129±9.331 | 193.554 ±7.155 | 0.000±0.000 | -8.721±13.304 |
| | PRO4 | 0.000±3.537 | -1.943±0.352 | -0.322±2.239 | 0.259±1.211 | 0.000±0.000 | -2.005±4.372 |
| | LEU5 | 0.000±4.324 | -0.060±0.911 | -0.200±2.150 | 0.170±1.353 | 0.000±0.000 | -0.090±5.097 |
| | ASP6 | 0.000±3.858 | -0.038±0.948 | 97.539±7.973 | -96.464 ±6.846 | 0.000±0.000 | 1.037±11.235 |
| | LYS7 | 0.000±4.463 | -1.365±1.212 | -137.473±12.109 | 135.368 ±11.138 | 0.000±0.000 | -3.471±17.235 |
| | LYS8 | 0.000±5.097 | -0.273±1.277 | -133.693 ±10.440 | 132.024 ±7.395 | 0.000±0.000 | -1.942±13.831 |
| | AGR9 | 0.000±6.130 | -0.425±0.526 | -136.458 ±18.229 | 134.808 ±17.008 | 0.000±0.000 | -2.075±25.679 |
| | GLU10 | 0.000±4.135 | -0.017±0.441 | 94.888±7.018 | -93.786±6.304 | 0.000±0.000 | 1.085±10.310 |
| | GLU11 | 0.000±4.036 | -0.012±0.843 | 113.134±12.261 | -111.653±11.932 | 0.000±0.000 | 1.469±17.598 |
| | ALA12 | 0.000±3.037 | -0.002±0.300 | 1.847 ±2.421 | -1.817±0.996 | 0.000±0.000 | 0.027±4.043 |
| | PRO13 | 0.000±3.398 | -0.001±0.579 | 0.691 ±1.394 | -0.682±1.100 | 0.000±0.000 | 0.008±3.878 |
| | SER14 | 0.000±6.040 | -0.001±2.947 | 0.157±4.774 | -0.156±2.276 | 0.000±0.000 | 0.000±8.552 |
| | LEU15 | 0.000±4.606 | -0.010±0.824 | -2.041±2.101 | 2.002±1.128 | 0.000±0.000 | -0.048±5.252 |
| | ARG16 | 0.000±5.385 | -0.027±0.836 | -117.842±9.026 | 116.267±6.143 | 0.000±0.000 | -1.602±12.203 |
| | PRO17 | 0.000±3.553 | -0.002±0.261 | 3.681±1.775 | -3.629±1.646 | 0.000±0.000 | 0.050±4.307 |
| | ALA18 | 0.000±3.228 | -0.002±0.254 | -1.758±2.485 | 1.740±1.479 | 0.000±0.000 | -0.020±4.342 |
| | PRO19 | 0.000±3.361 | -0.005±0.477 | -2.620±1.961 | 2.585±1.157 | 0.000±0.000 | -0.040 ±4.088 |
| | PRO20 | 0.000±3.306 | -0.002±0.451 | 2.403±1.960 | -2.376±1.310 | 0.000±0.000 | 0.025±4.085 |
| | PRO21 | 0.000±3.383 | -0.001±0.509 | 1.146±1.223 | -1.131±1.023 | 0.000±0.000 | 0.014 ±3.775 |
| | ILE22 | 0.000±4.600 | -0.001±1.439 | 0.626±1.955 | -0.615±0.977 | 0.000±0.000 | 0.010 ±5.292 |
| | SER23 | 0.000±4.178 | -0.003±1.262 | -1.245±3.733 | 1.227±1.903 | 0.000±0.000 | -0.020 ±6.050 |
| | GLY24 | 0.000±2.883 | -0.003±0.232 | 2.108±3.355 | -2.072±1.376 | 0.000±0.000 | 0.033 ±4.638 |
| | GLY25 | 0.000±2.907 | -0.006±0.493 | 3.638±2.714 | -3.587±1.635 | 0.000±0.000 | 0.045 ±4.238 |
| | GLY26 | 0.000±2.559 | -0.007±0.937 | 2.936±1.810 | -2.885±1.474 | 0.000±0.000 | 0.045±3.588 |
| | TYR27 | 0.000±4.631 | -0.020±0.896 | 2.506±3.207 | -2.486±1.914 | 0.000±0.000 | 0.000±6.017 |
| | ARG28 | 0.000±5.970 | 5.430±13.635 | -67.220±9.105 | -66.588 ±5.872 | 0.000±0.000 | 4.798±18.410 |

Table S5. The pairwise decomposition of binding energy.

| Residue pair | Internal (kcal/mol) | van der Waals (kcal/mol) | Electrostatics (kcal/mol) | Polar Solvation (kcal/mol) | Non-polar Solvation (kcal/mol) | Total (kcal/mol) |
|--------------|------------------------|-----------------------------|------------------------------|----------------------------------|--------------------------------------|---------------------|
| HEP:GLY1 | 0.000±0.000 | 1.762±5.700 | -199.613±9.094 | 187.402±7.160 | 0.000±0.000 | -10.449±12.901 |
| HEP:HIE2 | 0.000±0.000 | -1.500±0.191 | 6.783±2.153 | -8.360±1.852 | 0.000±0.000 | -3.077±2.846 |
| HEP:ARG3 | 0.000±0.000 | -2.146±0.397 | -200.129±6.061 | 185.098±4.187 | 0.000±0.000 | -17.176±7.377 |
| HEP:PRO4 | 0.000±0.000 | -1.943±0.245 | -0.322±0.887 | 0.284±0.781 | 0.000±0.000 | -1.980±1.207 |
| HEP:LEU5 | 0.000±0.000 | -0.060±0.009 | -0.200±0.703 | 0.203±0.691 | 0.000±0.000 | -0.057±0.986 |
| HEP:ASP6 | 0.000±0.000 | -0.038±0.005 | 97.539±2.203 | -96.464±2.175 | 0.000±0.000 | 1.031±3.096 |
| HEP:LYS7 | 0.000±0.000 | -1.365±0.372 | -137.473±14.351 | 131.581±12.403 | 0.000±0.000 | -7.258±18.972 |
| HEP:LYS8 | 0.000±0.000 | -0.273±0.073 | -133.693±3.390 | 131.298±3.244 | 0.000±0.000 | -2.668±4.692 |
| HEP:AGR9 | 0.000±0.000 | -0.425±0.259 | -136.458±20.459 | 133.812±19.252 | 0.000±0.000 | -3.071±28.094 |
| HEP:GLU10 | 0.000±0.000 | -0.017±0.005 | 94.888±5.505 | -93.778±5.411 | 0.000±0.000 | 1.093±7.719 |
| HEP:GLU11 | 0.000±0.000 | -0.012±0.002 | 113.134±4.059 | -111.559±3.945 | 0.000±0.000 | 1.564±5.660 |
| HEP:ALA12 | 0.000±0.000 | -0.002±0.001 | 1.847±0.526 | -1.813±0.515 | 0.000±0.000 | 0.031±0.736 |
| HEP:PRO13 | 0.000±0.000 | -0.001±0.000 | 0.691±0.456 | -0.686±0.450 | 0.000±0.000 | 0.004±0.641 |
| HEP:SER14 | 0.000±0.000 | -0.001±0.000 | 0.157±1.091 | -0.158±1.073 | 0.000±0.000 | -0.002±1.530 |
| HEP:LEU15 | 0.000±0.000 | -0.010±0.003 | -2.041±0.580 | 1.995±0.566 | 0.000±0.000 | -0.055±0.810 |
| HEP:ARG16 | 0.000±0.000 | -0.027±0.005 | -117.842±3.041 | 116.076±2.950 | 0.000±0.000 | -1.793±4.237 |
| HEP:PRO17 | 0.000±0.000 | -0.002±0.000 | 3.681±0.333 | -3.628±0.325 | 0.000±0.000 | 0.050±0.465 |
| HEP:ALA18 | 0.000±0.000 | -0.002±0.000 | -1.758±0.406 | 1.744±0.401 | 0.000±0.000 | -0.016±0.571 |
| HEP:PRO19 | 0.000±0.000 | -0.005±0.001 | -2.620±0.491 | 2.580±0.483 | 0.000±0.000 | -0.045±0.689 |
| HEP:PRO20 | 0.000±0.000 | -0.002±0.000 | 2.403±0.307 | -2.379±0.303 | 0.000±0.000 | 0.022±0.431 |
| HEP:PRO21 | 0.000±0.000 | -0.001±0.000 | 1.146±0.479 | -1.134±0.475 | 0.000±0.000 | 0.011±0.674 |
| HEP:ILE22 | 0.000±0.000 | -0.001±0.000 | 0.626±0.316 | -0.620±0.312 | 0.000±0.000 | 0.005±0.444 |
| HEP:SER23 | 0.000±0.000 | -0.003±0.001 | -1.244±0.713 | 1.223±0.702 | 0.000±0.000 | -0.025±1.000 |
| HEP:GLY24 | 0.000±0.000 | -0.003±0.001 | 2.108±0.470 | -2.056±0.463 | 0.000±0.000 | 0.048±0.660 |
| HEP:GLY25 | 0.000±0.000 | -0.006±0.002 | 3.638±1.803 | -3.585±1.772 | 0.000±0.000 | 0.047±2.529 |
| HEP:GLY26 | 0.000±0.000 | -0.007±0.002 | 2.936±1.323 | -2.893±1.301 | 0.000±0.000 | 0.037±1.856 |
| HEP:TYR27 | 0.000±0.000 | -0.020±0.003 | 2.506±0.831 | -2.439±0.809 | 0.000±0.000 | 0.047±1.160 |
| HEP:ARG28 | 0.000±0.000 | 5.430±13.553 | -67.220±7.684 | 55.451±4.300 | 0.000±0.000 | -6.339±16.162 |

References and Notes

1. Bishop, J.R., Schuksz, M. & Esko, J.D. Heparan sulphate proteoglycans fine-tune mammalian physiology. *Nature* **446**, 1030-1037 (2007).
2. Linhardt, R.J. & Liu, J. Synthetic heparin. *Current Opinion in Pharmacology* **12**, In press (2012).
3. Stevenson, J.L., Choi, S.H. & Varki, A. Differential metastasis inhibition by clinically relevant levels of heparins - Correlation with selectin inhibition, not antithrombotic activity. *Clin. Cancer Res.* **11**, 7003-7011 (2005).
4. Wang, L.C., Brown, J.R., Varki, A. & Esko, J.D. Heparin's anti-inflammatory effects require glucosamine 6-O-sulfation and are mediated by blockade of L- and P-selectins. *J. Clin. Invest.* **110**, 127-136 (2002).
5. Xu, Y.M. et al. Chemoenzymatic Synthesis of Homogeneous Ultralow Molecular Weight Heparins. *Science* **334**, 498-501 (2011).
6. Esko, J.D. & Selleck, S.B. Order out of chaos: Assembly of ligand binding sites in heparan sulfate. *Annu. Rev. Biochem.* **71**, 435-471 (2002).
7. Raman, R., Sasisekharan, V. & Sasisekharan, R. Structural insights into biological roles of protein-glycosaminoglycan interactions. *Chem. Biol.* **12**, 267-277 (2005).
8. Capila, I. & Linhardt, R.J. Heparin - Protein interactions. *Angew. Chem. Int. Ed.* **41**, 391-412 (2002).
9. Powell, A.K., Yates, E.A., Fernig, D.G. & Turnbull, J.E. Interactions of heparin/heparan sulfate with proteins: Appraisal of structural factors and experimental approaches. *Glycobiology* **14**, 17R-30R (2004).
10. Ibrahimi, O.A., Zhang, F.M., Hrstka, S.C.L., Mohammadi, M. & Linhardt, R.J. Kinetic model for FGF, FGFR, and proteoglycan signal transduction complex assembly. *Biochemistry* **43**, 4724-4730 (2004).
11. Keiser, N., Venkataraman, G., Shriver, Z. & Sasisekharan, R. Direct isolation and sequencing of specific protein-binding glycosaminoglycans. *Nat. Med.* **7**, 123-128 (2001).
12. Mulloy, B. & Linhardt, R.J. Order out of complexity - protein structures that interact with heparin. *Curr. Opin. Struc. Biol.* **11**, 623-628 (2001).

13. Pantoliano, M.W. et al. Multivalent Ligand-Receptor Binding Interactions in the Fibroblast Growth-Factor System Produce a Cooperative Growth-Factor and Heparin Mechanism for Receptor Dimerization. *Biochemistry* **33**, 10229-10248 (1994).
14. Sweeney, M.D., Yu, Y.H. & Leary, J.A. Effects of sulfate position on heparin octasaccharide binding to CCL2 examined by tandem mass spectrometry. *J. Am. Soc. Mass. Spectr* **17**, 1114-1119 (2006).
15. Wu, Z.L.L. et al. The involvement of heparan sulfate (HS) in FGF1/HS/FGFR1 signaling complex. *J. Biol. Chem.* **278**, 17121-17129 (2003).
16. Rogers, C.J. et al. Elucidating glycosaminoglycan-protein-protein interactions using carbohydrate microarray and computational approaches. *Proc. Natl. Acad. Sci. USA* **108**, 9747-9752 (2011).
17. Arungundram, S. et al. Modular Synthesis of Heparan Sulfate Oligosaccharides for Structure-Activity Relationship Studies. *J. Am. Chem. Soc.* **131**, 17394-17405 (2009).
18. Linhardt, R.J. & Kim, J.H. Combinatorial enzymatic synthesis of heparan sulfate. *Chem. Biol.* **14**, 972-973 (2007).
19. Zayats, M., Huang, Y., Gill, R., Ma, C.A. & Willner, I. Label-free and reagentless aptamer-based sensors for small molecules. *J. Am. Chem. Soc.* **128**, 13666-13667 (2006).
20. Abbondanzieri, E.A., Greenleaf, W.J., Shaevitz, J.W., Landick, R. & Block, S.M. Direct observation of base-pair stepping by RNA polymerase. *Nature* **438**, 460-465 (2005).
21. Asbury, C.L., Fehr, A.N. & Block, S.M. Kinesin moves by an asymmetric hand-over-hand mechanism. *Science* **302**, 2130-2134 (2003).
22. Liphardt, J., Dumont, S., Smith, S.B., Tinoco, I. & Bustamante, C. Equilibrium information from nonequilibrium measurements in an experimental test of Jarzynski's equality. *Science* **296**, 1832-1835 (2002).
23. Smith, S.B., Cui, Y.J. & Bustamante, C. Overstretching B-DNA: The elastic response of individual double-stranded and single-stranded DNA molecules. *Science* **271**, 795-799 (1996).
24. Bayas, M.V., Leung, A., Evans, E. & Leckband, D. Lifetime measurements reveal kinetic differences between homophilic cadherin bonds. *Biophys. J.* **90**, 1385-1395 (2006).

25. Evans, E., Ritchie, K. & Merkel, R. Sensitive Force Technique to Probe Molecular Adhesion and Structural Linkages at Biological Interfaces. *Biophys. J.* **68**, 2580-2587 (1995).
26. Merkel, R., Nassoy, P., Leung, A., Ritchie, K. & Evans, E. Energy landscapes of receptor-ligand bonds explored with dynamic force spectroscopy. *Nature* **397**, 50-53 (1999).
27. Muller, D.J. & Dufrene, Y.F. Atomic force microscopy as a multifunctional molecular toolbox in nanobiotechnology. *Nat. Nanotechnol.* **3**, 261-269 (2008).
28. Engel, A. & Muller, D.J. Observing single biomolecules at work with the atomic force microscope. *Nat. Struct. Biol.* **7**, 715-718 (2000).
29. Allison, D.P., Hinterdorfer, P. & Han, W.H. Biomolecular force measurements and the atomic force microscope. *Curr. Opin. Biotech.* **13**, 47-51 (2002).
30. Rief, M., Gautel, M., Oesterhelt, F., Fernandez, J.M. & Gaub, H.E. Reversible unfolding of individual titin immunoglobulin domains by AFM. *Science* **276**, 1109-1112 (1997).
31. Strick, T.R., Allemand, J.F., Bensimon, D., Bensimon, A. & Croquette, V. The elasticity of a single supercoiled DNA molecule. *Science* **271**, 1835-1837 (1996).
32. Tanaka, H. et al. The motor domain determines the large step of myosin-V. *Nature* **415**, 192-195 (2002).
33. Benoit, M., Gabriel, D., Gerisch, G. & Gaub, H.E. Discrete interactions in cell adhesion measured by single-molecule force spectroscopy. *Nat. Cell Biol.* **2**, 313-317 (2000).
34. Feklistov, A. & Darst, S.A. Structural Basis for Promoter-10 Element Recognition by the Bacterial RNA Polymerase sigma Subunit. *Cell* **147**, 1257-1269 (2011).
35. Kruse, A.C. et al. Structure and dynamics of the M3 muscarinic acetylcholine receptor. *Nature* **482**, 552-556 (2012).
36. Eltzschig, H.K. & Eckle, T. Ischemia and reperfusion-from mechanism to translation. *Nat. Med.* **17**, 1391-1401 (2011).
37. Jennewein, C., Paulus, P. & Zacharowski, K. Linking inflammation and coagulation: novel drug targets to treat organ ischemia. *Current Opinion in Anesthesiology* **24**, 375-380 (2011).

38. Jennewein, C. et al. Novel Aspects of Fibrin(ogen) Fragments during Inflammation. *Mol. Med.* **17**, 568-573 (2011).
39. Krishnamoorthy, A. et al. Fibrinogen beta-derived B beta(15-42) peptide protects against kidney ischemia/reperfusion injury. *Blood* **118**, 1934-1942 (2011).
40. Matt, U. et al. B beta(15-42) Protects against Acid-induced Acute Lung Injury and Secondary Pseudomonas Pneumonia In Vivo. *Am. J. Resp. Crit. Care* **180**, 1208-1217 (2009).
41. Petzelbauer, P. et al. The fibrin-derived peptide B beta(15-42) protects the myocardium against ischemia-reperfusion injury. *Nat. Med.* **11**, 298-304 (2005).
42. Atar, D. et al. Effect of Intravenous FX06 as an Adjunct to Primary Percutaneous Coronary Intervention for Acute ST-Segment Elevation Myocardial Infarction Results of the FIRE (Efficacy of FX06 in the Prevention of Myocardial Reperfusion Injury) Trial. *J. Am. Coll. Cardiol.* **53**, 720-729 (2009).
43. Bach, T.L., Barsigian, C., Yaen, C.H. & Martinez, J. Endothelial cell VE-cadherin functions as a receptor for the beta 15-42 sequence of fibrin. *J. Biol. Chem.* **273**, 30719-30728 (1998).
44. Bunce, L.A., Sporn, L.A. & Francis, C.W. Endothelial-Cell Spreading on Fibrin Requires Fibrinopeptide-B Cleavage and Amino-Acid-Residues 15-42 of the Beta Chain. *J. Clin. Invest.* **89**, 842-850 (1992).
45. Chalupowicz, D.G., Chowdhury, Z.A., Bach, T.L., Barsigian, C. & Martinez, J. Fibrin-Ii Induces Endothelial-Cell Capillary-Tube Formation. *J. Cell Biol.* **130**, 207-215 (1995).
46. Hamaguchi, M., Bunce, L.A., Sporn, L.A. & Francis, C.W. Spreading of Platelets on Fibrin Is Mediated by the Amino Terminus of the Beta-Chain Including Peptide-Beta-15-42. *Blood* **81**, 2348-2356 (1993).
47. Odrlic, T.M. et al. Heparin-binding domain of fibrin mediates its binding to endothelial cells. *Arterioscl. Throm. Vas* **16**, 1544-1551 (1996).
48. Ribes, J.A., Ni, F., Wagner, D.D. & Francis, C.W. Mediation of Fibrin-Induced Release of Vonwillebrand-Factor from Cultured Endothelial-Cells by the Fibrin Beta-Chain. *J. Clin. Invest.* **84**, 435-442 (1989).

49. Sporn, L.A., Bunce, L.A. & Francis, C.W. Cell-Proliferation on Fibrin - Modulation by Fibrinopeptide Cleavage. *Blood* **86**, 1802-1810 (1995).
50. Lofas, S. Dextran Modified Self-Assembled Monolayer Surfaces for Use in Biointeraction Analysis with Surface-Plasmon Resonance. *Pure Appl. Chem.* **67**, 829-834 (1995).
51. Wang, B., Guo, C.L., Chen, G.J., Park, B. & Xu, B.Q. Following aptamer-ricin specific binding by single molecule recognition and force spectroscopy measurements. *Chem. Commun.* **48**, 1644-1646 (2012).
52. Horcas, I. et al. WSXM: A software for scanning probe microscopy and a tool for nanotechnology. *Rev. Sci. Instrum.* **78**, 013705 (2007).
53. Khan, S., Gor, J., Mulloy, B. & Perkins, S.J. Semi-Rigid Solution Structures of Heparin by Constrained X-ray Scattering Modelling: New Insight into Heparin-Protein Complexes. *J. Mol. Biol.* **395**, 504-521 (2010).
54. Trott, O. & Olson, A.J. AutoDock Vina: Improving the Speed and Accuracy of Docking with a New Scoring Function, Efficient Optimization, and Multithreading. *J. Comput. Chem.* **31**, 455-461 (2010).
55. Humphrey, W., Dalke, A. & Schulten, K. VMD: Visual molecular dynamics. *J. Mol. Graph. Model.* **14**, 33-38 (1996).
56. Dupradeau, F.Y. et al. The RED. tools: advances in RESP and ESP charge derivation and force field library building. *Phys. Chem. Chem. Phys.* **12**, 7821-7839 (2010).
57. Vanquelef, E. et al. RED Server: a web service for deriving RESP and ESP charges and building force field libraries for new molecules and molecular fragments. *Nucleic Acids Res.* **39**, W511-W517 (2011).
58. Frisch, M.J. et al., Gaussian 09, Revision A.02. Gaussian, Inc., Wallingford, CT; (2009).
59. Case, D.A. et al. AMBER 11. University of California, San Francisco, (2010).